Boundary-layer turbulence in experiments of quasi-Keplerian flows

By JOSE M. LOPEZ,[1,2,3] and MARC AVILA[1,4]

[1]Institute of Fluid Mechanics, Friedrich-Alexander-Universität Erlangen-Nürnberg, 91058 Erlangen, Germany

[2]Departament de Física Aplicada, Univ. Politècnica de Catalunya, Barcelona 08034, Spain

[3] Institute of Science and Technology, 3400 Klosterneuburg, Austria

[4] Center of Applied Space Technology and Microgravity, University of Bremen, 28359 Bremen, Germany

(Printed 23 February 2017)

Most flows in nature and engineering are turbulent because of their large velocities and spatial scales. Laboratory experiments of rotating quasi-Keplerian flows, for which the angular velocity decreases radially but the angular momentum increases, are however laminar at Reynolds numbers exceeding one million. This is in apparent contradiction to direct numerical simulations showing that in these experiments turbulence transition is triggered by the axial boundaries. We here show numerically that as the Reynolds number increases turbulence becomes progressively confined to the boundary layers and the flow in the bulk fully relaminarizes. Our findings support that turbulence is unlikely to occur in isothermal constant density quasi-Keplerian flows.

1. Introduction

Understanding the origin of turbulence in accretion disks is a long-standing problem in astrophysics (Ji & Balbus 2013). The simplest model for the flow of gas in an accretion disk consists of an isothermal incompressible constant density fluid rotating with a Keplerian angular velocity $\Omega \propto r^{-3/2}$, where r is the distance to the accreting central object. Despite the hydrodynamic stability of such flows to small disturbances (Rayleigh 1917), the possibility of a nonlinear transition to turbulence via finite-amplitude disturbances is not precluded. However, this has not been demonstrated and so several mechanisms capable of destabilizing Keplerian flows have been proposed in the literature (see Turner *et al.* 2014, for a recent review). Prominent amongst these is the magnetorotational instability (MRI, see Balbus & Hawley 1998; Balbus 2003), which can drive vigorous turbulence and transport angular momentum at rates required for accretion to occur. However, the MRI operates in ionized disks only and so it does not apply to cool protostellar disks. There are many mechanisms that might give rise to turbulence in the absence of magnetic fields: baroclinic instabilities (Klahr & Bodenheimer 2003; Johnson

& Gammie 2006; Petersen *et al.* 2007), instabilities driven by radial (Goldreich & Schubert 1967; Fricke 1968; Urpin & Brandenburg 1998) or axial stratification (Shalybkov & Rüdiger 2005; Dubrulle *et al.* 2005*b*; Marcus *et al.* 2015), crossflow instabilities (Kerswell 2015), convective instabilities (Lin & Papaloizou 1980; Ryu & Goodman 1992) or self-gravitation (Toomre 1964; Lin & Pringle 1987). Nevertheless, their applicability to accretion disks is still under investigation. Whereas there is an understanding of the underlying instability mechanisms, their non-linear evolution and saturated state have still to be studied in realistic disk simulations with the proper radiation transport and analysing the effect of the boundary conditions.

In general, the lack of observational evidence and the computational limitations in simulating the extreme parameter values governing the dynamics of accretion disks makes them a particularly difficult object to study (see e.g. Miesch *et al.* 2015). This has motivated the development of laboratory experiments capturing the essential physics at play. Quasi-Keplerian flows, for which the angular velocity decreases radially, whereas the angular momentum increases, can in principle be realized in laboratory experiments of fluids between two concentric rotating cylinders (Taylor–Couette flow). If the cylinders are assumed to be infinite in length the basic laminar flow is purely azimuthal

$$v(r) = \frac{\Omega_o r_o^2 - \Omega_i r_i^2}{r_o^2 - r_i^2} r + \frac{(\Omega_i - \Omega_o)(r_i r_o)^2}{r_o^2 - r_i^2} \frac{1}{r}, \tag{1.1}$$

where Ω_i (Ω_o) and r_i (r_o) are the angular velocity and radius of the inner (outer) cylinder. Provided that $\Omega_i > \Omega_o$ but $r_i^2\Omega_i < r_o^2\Omega_o$ then the basic *Couette* flow (1.1) is quasi-Keplerian. Despite the apparent simplicity of this model, laboratory realizations of quasi-Keplerian velocity profiles are fraught with difficulty. In practice, the viscous interaction between fluid and end-plates confining the fluid in the axial direction results in secondary flows, also known as Ekman circulation (EC). EC can extend deep into the bulk flow and cause the azimuthal velocity to significantly deviate from the theoretical profile (1.1) as the rotation speeds increase (Richard & Zahn 1999; Hollerbach & Fournier 2004).

Pioneering experiments of quasi-Keplerian flows were conducted by Ji *et al.* (2006), who used a short height-to-gap aspect ratio and end plates split into two independently rotating rings. Ji *et al.* (2006) carefully adjusted the rotation speed of the rings so as to minimize EC and measured Reynolds stresses in the bulk. They concluded that the bulk flow was laminar despite reaching Reynolds numbers of up to 10^6. These results were questioned by Paoletti & Lathrop (2011), who used a tall apparatus with end plates attached to the outer cylinder. Paoletti & Lathrop (2011) split the inner cylinder vertically in three sections and measured the torque on the central section so as to reduce the effect of the end plates in their measurements. However, Avila (2012) performed direct numerical simulations reproducing the precise geometry of Ji *et al.* (2006) and Paoletti & Lathrop (2011) and showed that in both setups strong EC render the flows turbulent at Reynolds numbers as low as 10^3. Although his simulations were consistent with the turbulent flows observed by Paoletti & Lathrop (2011), as confirmed by subsequent ex-

periments (Nordsiek *et al.* 2015), they were in apparent contradiction with the laminar flows observed by Ji *et al.* (2006).

More recently, Edlund & Ji (2014) attributed this discrepancy to the large gap in Reynolds numbers between simulations and experiments. They directly measured velocity profiles in a new experimental setup and showed that if the end plates are rotated within a certain range of velocities, hereafter referred to as optimal boundary conditions, quasi-Keplerian Couette flow (1.1) is obtained and remains stable even when subject to strong disturbances.

We here perform direct numerical simulations of experimental quasi-Keplerian flows for Reynolds numbers up to $50,000$. We show that as the Reynolds number increases, turbulence becomes progressively confined to thin boundary layers at the end plates. As a result laminar quasi-Keplerian profiles are realized in the bulk of the experiment. We provide a detailed picture of the relaminarisation process and the role of the boundary conditions for two distinct configurations studied by Edlund & Ji (2015). Our results bridge the gap between experiments and previous simulations and support the experimental conclusion that constant density isothermal quasi-Keplerian Taylor–Couette flows are stable.

2. Specification of the problem and numerical methods

A fluid of kinematic viscosity ν is contained in the annular gap between two vertical concentric cylinders of length h and radii r_i and r_o. The subindex i (o) denotes the inner (outer) cylinder and $d = r_o - r_i$ is the gap width. Differential rotation is generated by rotating the cylinders at independent angular velocities Ω_i and Ω_o. The shear Reynolds number, R_s, and the rotation number, R_Ω, were chosen as control parameters

$$R_s = \frac{\tilde{S} d^2}{\nu}, \qquad R_\Omega = \frac{2\tilde{\Omega}}{\tilde{S}}, \tag{2.1}$$

where $\tilde{S}$ and $\tilde{\Omega}$ are the shear and rotation speed of the basic Couette flow (1.1) evaluated at the mean geometric radius $\tilde{r} = \sqrt{r_i r_o}$. The rotation number allows for a clear distinction between cyclonic ($R_\Omega > 0$) and anticyclonic ($R_\Omega < 0$) flows. It has been widely used to characterize different rotation regimes of the Taylor–Couette experiments and to compare results for different geometries (Dubrulle *et al.* 2005*a*; Ravelet *et al.* 2010; Paoletti *et al.* 2012).

In astrophysics $q = -\frac{d \ln \Omega}{d \ln r}$ is used to characterise the rotation law. The flow is quasi-Keplerian if R_Ω (q) is chosen within the range $-\infty < R_\Omega < -1$ ($0 < q < 2$). In the simulations presented in this paper, $R_\Omega = -1.038$ ($q = 1.93$) was chosen, corresponding to the experiments of Ji *et al.* (2006) and simulations of Avila (2012), and close to the value $q = 1.8$ chosen by Edlund & Ji (2014). Their apparatus is axially bounded by two horizontal plates which rotate differentially with respect to the cylinders. These end plates can be further split into several independently rotating rings whose angular velocities can be adjusted to best approximate (1.1). The geometry of their apparatus

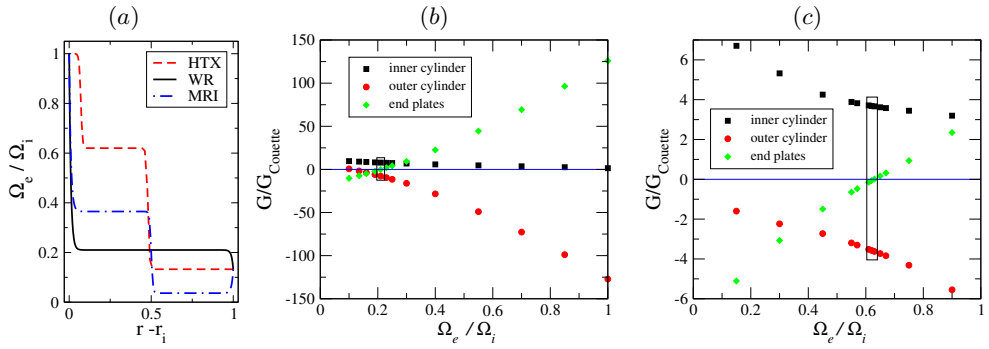

FIGURE 1. (a) Rotation speed of the end plates (Ω_e) normalised by the rotation speed of the inner cylinder (Ω_i) in the *WR*, *HTX* and *MRI* configurations. (b) Torque (G) on the cylinders and end plates in the the *WR* configuration as a function of Ω_e. G is normalised by the torque of the Couette profile (1.1) (G_{Couette}). The optimal rotation range is enclosed in a rectangular box. (c) Same as in (b) for the *HTX* configuration. In both (b) and (c) torques were computed at $R_s = 644$.

is fully specified by two dimensionless parameters: the radius ratio, $\eta = r_i/r_o = 0.3478$, and the length-to-gap aspect ratio, $\Gamma = h/d = 2.1$.

Different configurations of this apparatus differ from one another in the number of rings into which the end plates are split. Here, we study in detail two configurations, the so-called *HTX* and *wide ring* (*WR*), in which only one ring rotates differentially with respect to the cylinders. In the *HTX* configuration (dashed line in figure 1 (a)) the end plates are split in three rings. The inner and outer rings are attached to the cylinders, whereas the central ring rotates at an angular velocity Ω_e intermediate to those of the cylinders. In the *WR* configuration (solid line in figure 1 (a)) there is a single ring that spans the entire annulus but also rotates independently. The dot-dashed line in figure 1 (a) illustrates the boundary conditions of Ji *et al.* (2006), who designed their device to study the magnetorotational instability by using electrically conducting fluids and an imposed axial magnetic field. We will refer to this configuration as *MRI*.

2.1. *Numerical method*

The Navier–Stokes equations have been solved in cylindrical coordinates using a second order time-splitting method (Hughes & Randriamampianina 1998; Mercader *et al.* 2010). The spatial discretization is via a Galerkin-Fourier expansion in θ and Chebyshev collocation in r and z. Hereafter the radial u, azimuthal v and axial w velocities are normalized with respect to the characteristic velocity $\tilde{S}d$ used in the definition of the shear Reynolds number (2.1). The code used is a parallelized version of a spectral solver that has been widely tested (Avila *et al.* 2008; Lopez & Marques 2015; Lopez *et al.* 2015). Details of the parallelization strategy can be found in Shi *et al.* (2015).

In the *WR* and *HTX* configurations there are discontinuities in the angular velocity at the junctions where elements rotating at different speeds meet. For an accurate use of spectral techniques these discontinuities must be regularised (see Lopez & Shen (1998)). In the *WR* configuration this is accomplished through the introduction of two exponential

Configuration	L	N	M	R_s
WR	128	256	544	47630
HTX	392	642	224	32180
MRI	192	192	288	12874

TABLE 1. Maximum spatial resolution and R_s for each configuration. L,N and M indicate the number of spectral modes in the radial, azimuthal and axial directions, respectively.

functions in the form

$$\Omega(r) = \Omega_e + (\Omega_o - \Omega_e)e^{-(r-r_o)/\epsilon} + (\Omega_i - \Omega_e)e^{(r-r_i)/\epsilon}, \tag{2.2}$$

whereas in the *HTX* configuration two hyperbolic tangent functions are used

$$\Omega(r) = 0.5(\Omega_i + \Omega_o + (\Omega_o - \Omega_e)\ \tanh((r - \hat{r_o})/\epsilon) + (\Omega_e - \Omega_i)\ \tanh((r - \hat{r_i})/\epsilon)), \tag{2.3}$$

where $\hat{r_o} = r_i + 0.48$ and $\hat{r_i} = r_i + 0.071$ are the radial locations at which the central ring meets the outer and inner rings respectively. In both cases $\epsilon = 0.01$ was used.

The numerical resolution was carefully chosen in order to meet several requirements. First, we checked that the total angular momentum flux through cylinders and end plates vanished in the statistically stationary regime. Second, we gradually increased the number of collocation points until converged values of the torque at the inner and outer cylinders were obtained. Finally, we checked the spectral convergence of the code using the infinity norm of the spectral coefficients of the computed solutions, defined as $||a_l||_\infty = \max_{n,m} |a_{l,n,m}|$ for the radial direction, and analogously for the axial and azimuthal directions. An example of spatial convergence is illustrated in figure 2, which shows $||a_j||_\infty$, with $j = l, n, m$, of the radial velocity u for a solution corresponding to the *HTX* configuration at $R_s = 25747$. This solution was computed with $L = 360$ and $N = 221$ Chebyshev axial points in r and z, and $M = 320$ Fourier modes in θ. In all simulations the trailing coefficients of the spectral expansion were at least four orders of magnitude smaller than the leading coefficients. Table 1 shows the spatial resolution corresponding to the largest R_s simulated for each configuration. The reader is referred to Brauckmann & Eckhardt (2013) for a comprehensive analysis on the suitability of these convergence criteria for Taylor–Couette flows at large Reynolds numbers.

2.2. *Optimal boundary conditions*

Following Edlund & Ji (2015), we here determine the optimal rotation speed of the end plates from a balance of the angular momentum fluxes (torque) through the boundaries of the apparatus. In particular, optimal rotation is identified when the torque at the end plates (G_e) becomes zero, so that the torque on the cylinders has the same magnitude

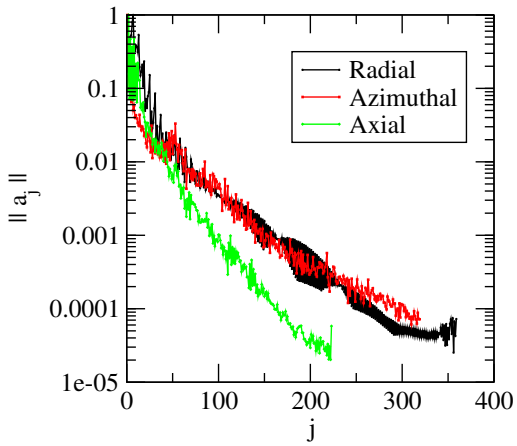

FIGURE 2. Convergence of the spectral coefficients of the radial velocity u in the three spatial directions using the infinity norm. It corresponds to a simulation of the HTX configuration at $R_s = 25747$. This solution has been computed with $L = 360$ Chebyshev radial points, $M = 320$ Fourier modes and $N = 221$ Chebyshev axial points.

but opposite sign, $G_i = -G_o$, as in the infinite-cylinder idealization. Figures 1 (b) and (c) show the torque across the cylinders and end plates as a function of Ω_e for solutions computed at $R_s = 644$ in both configurations. In agreement with Edlund & Ji (2015), in both cases there exist a narrow range of Ω_e for which $G_e = 0$ is approximately fulfilled (rectangular box in figures 1 (b) and (c)). For our simulations we chose $\Omega_e = 0.62\Omega_i$ (HTX) and $\Omega_e = 0.21\Omega_i$ (WR). Note that the torque in the WR configuration is substantially larger than in the HTX setup. The reason for this will be discussed in §3, along with the description of the secondary flows in both setups.

3. Basic flow and transition to turbulence

3.1. *Wide ring*

Figure 3 (a) shows that in the WR configuration the secondary EC cells extend over the entire annulus. Near the end plates, the flow is deflected radially towards the cylinders leading to two Ekman vortices with opposite sense of circulation. The size and intensity of these vortices change with Ω_e and it is only under optimal boundary conditions that these have nearly equal size and strength ($\max|u| = 0.08$). When the fluid reaches the cylinders it is transported from the end plates to the mid-plane over Stewartson boundary layers. As a result, two strong radial jets emerge from the cylinders and displace the flow towards mid-gap. The circulation cycle is then closed by two vertical cells that transport the fluid back to the end plates.

These large-scale secondary flows lead to linear instabilities that manifest themselves at the equatorial region (Avila *et al.* 2008; Avila 2012), and cause a transition to turbulence at low values of R_s. Figure 4 (a) shows, through isosurfaces of the radial velocity u, the location of the most unstable mode at the onset of instability. Note that the axisymmetric

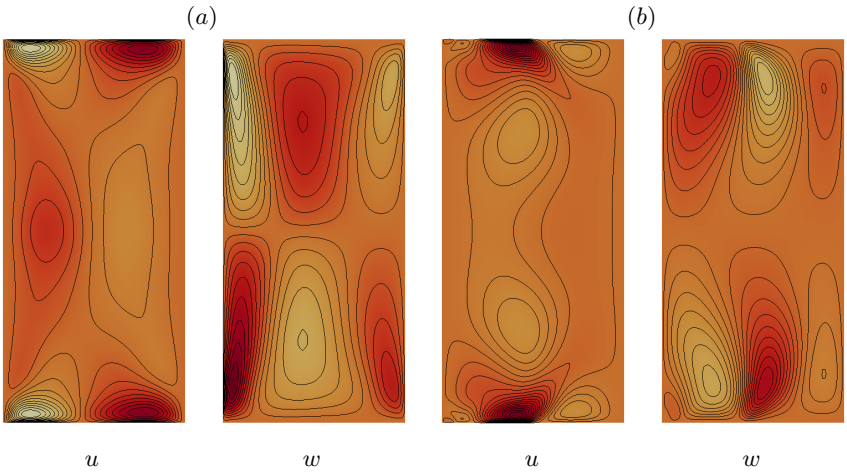

FIGURE 3. Meridional sections (r, z) showing color maps of the radial (left panel) and axial (right panel) velocities in the *WR* (a) and *HTX* (b) configurations. The solutions depicted correspond in both cases to laminar flow computed at $Re_s = 644$. In all figures shown in this paper, dark (light) regions indicate zones of positive (negative) velocities. There are 20 contours equally distributed in $u \in [-0.08, 0.06]$, $w \in [-0.11, 0.11]$ and $u \in [-0.02, 0.08]$, $w \in [-0.07, 0.07]$ for the *WR* and *HTX* configurations respectively.

part of u has been subtracted to facilitate visualization. The flow pattern emerging from this primary transition, which takes place at $R_s \approx 865$, is a rotating wave with azimuthal wave number $m = 2$. As R_s is further increased, the flow undergoes secondary instabilities leading to either rotating waves with different m or quasi-periodic states, and becomes eventually turbulent at $R_s \approx 3218$. Figure 4 (c) shows isosurfaces of u for a turbulent state computed at $R_s = 3862$. Interestingly, the turbulence does not extend towards the end plates but remains concentrated around the mid-plane.

3.2. *HTX*

Figure 3 (b) shows that in the *HTX* configuration the secondary EC is mainly confined to the vicinity of the end plates. Because of the split end plates, the radial flow along them is arranged in four alternating outward-inward vortices which direct the flow towards the junctions between the rings. The pair of vortices located at the outermost part of the end plates are significantly larger and more intense ($\max|u| = 0.08$) than those arising near the inner cylinder ($\max|u| = 0.02$). Significant axial transport of fluid towards the mid-plane occurs only in a narrow region around mid-gap. However, the flow does not reach the mid-plane, as it is recirculated towards the inner cylinder by a strong radial inflow that arise at an approximately intermediate distance between the end plates and the equatorial region. Finally, the flow is pushed back towards the end plates by axial velocities arising in the regions near the cylinders. A comparison with the *WR* configuration reveals that the substantial difference in torque shown in section 2.2 is caused by the influence of the Stewartson boundary layers that form at the cylinders in the *WR* configuration.

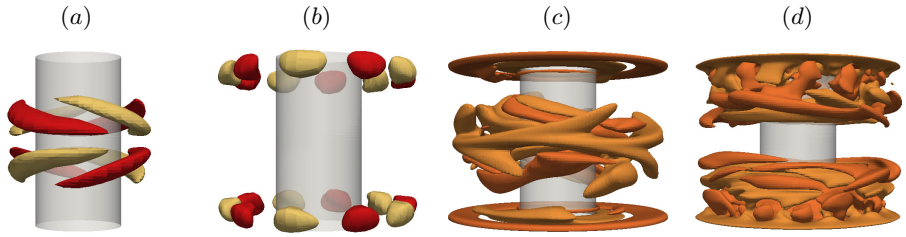

FIGURE 4. (*a*) and (*b*) show isosurfaces of the radial velocity of the leading eigenmodes near the onset of instability. The axisymmetric component has been subtracted to facilitate visualization of the spatial structure of the unstable mode. (*a*) Equatorial rotating wave with $m = 2$ computed at $R_s = 772$ in the *WR* configuration, (*b*) Rotating wave with $m = 5$ localised near the end plates for $R_s = 901$ in the *HTX* configuration. (*c*) and (*d*) show isosurfaces of the radial velocity for turbulent states computed at $R_s = 3862$ in the *WR* (*c*) and *HTX* (*d*) configurations. There are 6 isosurfaces equally distributed across $u \in [-0.13, 0.12]$ and $u \in [-0.09, 0.14]$ in the *WR* and *HTX* configurations respectively.

These produce strong azimuthal velocity gradients near the cylinders, which result in a significant increase of the torque as compared with that in the *HTX* configuration.

The meridional circulation in the HTX configuration becomes unstable at $R_s \approx 727$. The instability results in a rotating wave with $m = 5$ localised at the end plates (see figure 4 (*b*)), and the flow becomes quickly chaotic as R_s is increased ($R_s \approx 1287$). Nevertheless, the turbulence remains primarily localised near the upper and lower third of the experiment (see figure 4 (*d*)), so that the zonal flow at the equatorial region is barely affected by the secondary flows and nearly matches a quasi-Keplerian velocity profile, see §4.2.

4. Dynamics at high Reynolds numbers

As the rotation of the cylinders is increased the spatial arrangement of the secondary flows undergo significant changes in both configurations, which alter the structure of the resulting turbulence. While this transition occurs smoothly with increasing R_s, we here distinguish between low and high Reynolds numbers using $R_s \approx 10^4$ as an approximate threshold, beyond which the changes described in this section begin to become apparent.

4.1. *Wide ring*

Figure 5 (*a*) shows the structure of the time-averaged secondary flow for the *WR* configuration at $R_s = 19302$. Here the radial jets that emanate from the cylinders at the equatorial region do not extend across the entire gap, but remain localised in regions closer to the cylinders. The gradual displacement of these jets towards the cylinders as R_s increases is accompanied by the emergence of two pairs of radial flow cells on top and bottom of them. These radial cells recirculate the flow towards the cylinders, so that the vertical transport of fluid from the equator towards the end plates that closes the Ekman circulation cycle is also confined to the vicinity of the cylinders. As a result, the

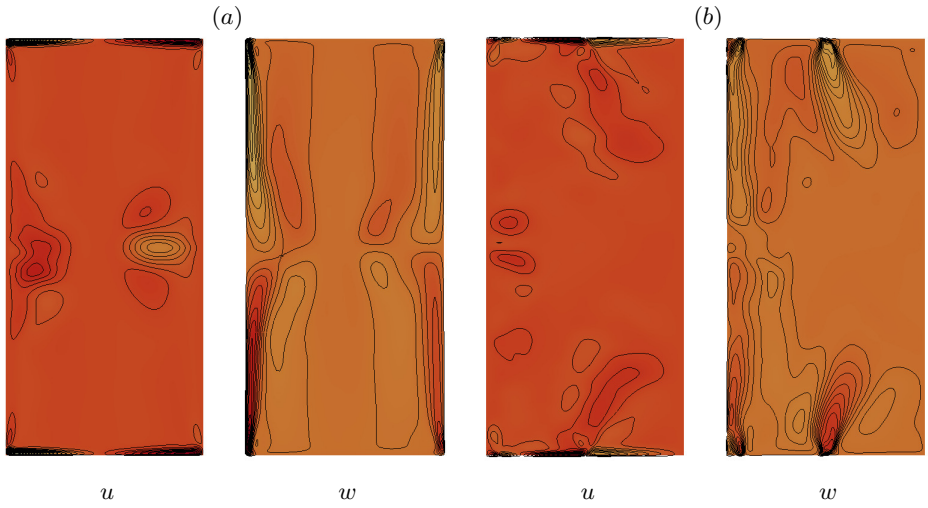

FIGURE 5. Meridional sections (r, z) showing color maps of the mean radial (left panel) and axial (right panel) velocities in the *WR* (a) and *HTX* (b) configurations. The solutions depicted were computed at $R_s = 19310$ in (a) and $R_s = 22529$ in (b). There are 20 contours equally distributed in $u \in [-0.16, 0.08]$, $w \in [-0.17, 0.17]$ and $u \in [-0.07, 0.10]$, $w \in [-0.06, 0.06]$ for the *WR* and *HTX* configurations respectively.

radial and axial velocities are nearly zero over the central region of the gap and the flow becomes essentially azimuthal in the bulk, resulting in vanishing Reynolds stresses.

The turbulent dynamics of this system is confined to the region in which the radial equatorial jets penetrate into the bulk flow. Hence as R_s increases and the secondary flows occupy regions closer to the cylinders, significant turbulent fluctuations are only found in the vicinity of the cylinders. Figure 6 (a) clearly illustrates the progressive localisation of the turbulence near the cylinders as R_s increases. Interestingly, turbulent structures occur mainly near the inner cylinder, which could be related to the large curvature of the apparatus ($\eta = r_i/r_o = 0.3478$).

Figure 7 (a) shows the mean azimuthal velocity v for $R_s = 47630$. With the exception of the zones near the cylinders, where the flow is obviously affected by the turbulence, it is observed that v is nearly independent of the axial coordinate. This is confirmed in figure 7 (b), where $v(r)$ is shown at three different axial locations. Although these profiles collapse together, they differ substantially from the desired quasi-Keplerian velocity profile (1.1), shown as a (black) solid line in figure 7 (b). Interestingly, despite vanishing fluctuations (and hence Reynolds stresses) in the bulk, the profile is far from ideal because of the effect of the global EC.

4.2. *HTX*

Figure 5 (b) shows the structure of the time-averaged secondary meridional flow for the *HTX* configuration at $R_s = 22529$. As R_s increases both radial and axial velocities are progressively confined to the end plates, resulting in an increasingly larger region where the flow remains nearly purely azimuthal. There is a fraction of the secondary flow

(*a*) *WR*

$R_s = 11586$ $R_s = 27035$ $R_s = 47630$

(*b*) *HTX*

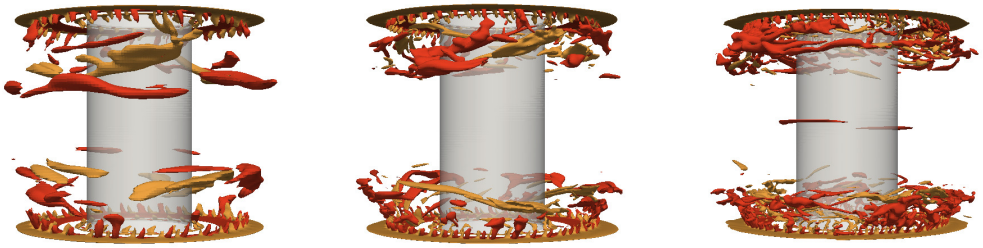

$R_s = 9655$ $R_s = 19310$ $R_s = 32180$

FIGURE 6. Evolution of the isosurfaces of the radial velocity u with R_s in both configurations. There are 2 isosurfaces corresponding to $u = \pm 0.04$ in both cases. Note that plots corresponding to the *WR* configuration are slightly tilted to better illustrate the gradual displacement of the turbulence towards the cylinders.

generated at the end plates that is transported to the equator over a boundary layer at the inner cylinder. The formation of this boundary layer leads to the emergence of two large-scale circulation cells, which are progressively confined to the inner cylinder as R_s is increased. These cells are similar to but significantly weaker than those in the *WR* configuration. Turbulent fluctuations are also progressively confined to the end plates as R_s increases (see figure 6 (*b*)). Some fluctuations caused by the large-scale recirculation flow may also occur in the vicinity of the inner cylinder. However, given their low intensity, it can be stated that the flow remains nearly laminar when sufficiently far from the end plates.

As seen in figure 7 (*c*), the mean azimuthal velocity is only significantly affected by the secondary flows in the vicinity of the end plates. Hence, negligible differences were found when measuring radial profiles of the mean azimuthal velocity in the bulk at different axial locations (see figure 7 (*c*)). Despite large-scale secondary flows develop at the inner cylinder, unlike for the *WR* configuration, these are not sufficiently strong as to significantly modify the azimuthal velocity. As a result, the azimuthal velocity profiles in this configuration closely approximate the desired quasi-Keplerian Couette flow (1.1). It should be noted that Edlund & Ji (2014) reported velocity profiles with a small but noticiable deviations from (1.1) near the inner cylinder. Such deviations suggest that,

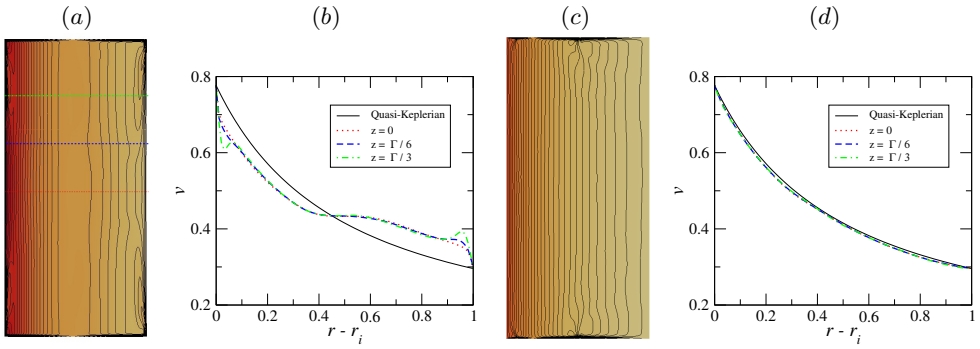

FIGURE 7. (*a*) and (*c*) show color maps and contours illustrating the mean azimuthal velocity v in the *WR* and *HTX* configurations respectively, whereas radial profiles of v computed at three different axial locations are shown in (*b*) *WR* and (*d*) *HTX*. In both cases the solution depicted corresponds to the maximum R_s achieved in our simulations, $R_s = 47630$ in (*a*) and (*b*), and $R_s = 32180$ in (*c*) and (*d*). There are 40 contours equally distributed across the full range of v. The (black) shows the quasi-Keplerian velocity profile (1.1) that would be achieved The horizontal lines superimposed upon figure (*a*) indicate the axial locations at which the azimuthal velocity profiles have been computed.

while the turbulence at the inner cylinder does not affect the bulk flow in our simulations, its influence might not be entirely negligible in experiments at larger R_s.

4.3. *Dynamics of the* MRI *configuration*

Avila (2012) performed direct numerical simulations of the *MRI* configuration of Ji *et al.* (2006) up to $R_s = 6437$, for which turbulence was found to fill the entire domain. Here we extend the range of Reynolds numbers by a factor of two. First of all, we note that the rotation speeds of the end-plate rings used by Ji *et al.* (2006) are not optimal and result in large torque at the end plates. At low R_s, the meridional circulation resembles that of the *WR* configuration (see figure 1 in Avila (2012)), with a strong radial jet located at the equatorial region. However, unlike the *WR*, the radial flow at the end plates is entirely inward, and so there is a single large-scale circulation cell in the upper and lower half of the experiment As in the *WR* configuration the large scale circulation cells and turbulent motions cluster here progressively near the inner cylinder (see figures 8 (*a*) and (*b*)), leaving a nearly azimuthal and laminar flow in the remaining part of the gap.

Figures 8 (*c*) and (*d*) show the time-averaged azimuthal velocity v and radial profiles of v at $R_s = 12874$ respectively. Here $v(r)$ is also nearly uniform in the axial direction, but differs from the theoretical Couette flow (1.1). Hence we conclude that although Ji *et al.* (2006) measured negligible Reynolds stresses in the bulk of their experiment, their flows were strongly turbulent in thin boundary layers at the cylinders. Interestingly, in the bulk the profiles are in fact quasi-Keplerian yet substantially shifted with respect to Couette flow because of the sharp drop at the cylinder boundary layers. Similar velocity profiles for this configuration were reported in the numerical simulations of Obabko *et al.* (2008) and experiments of Schartman *et al.* (2012), who speculated that the deviation in the

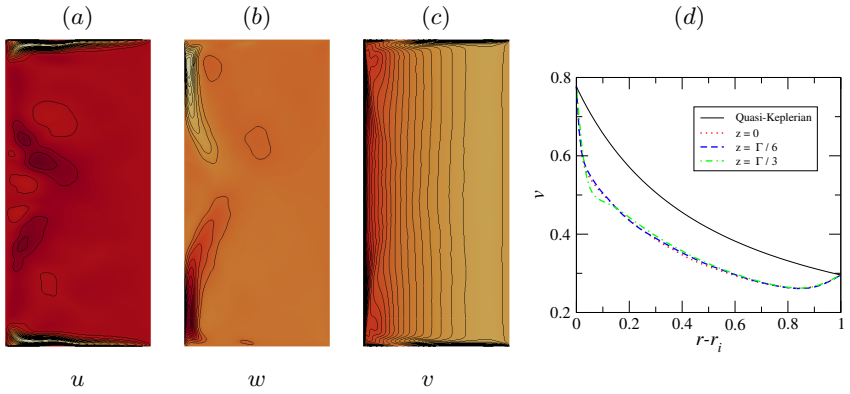

FIGURE 8. (*a*), (*b*) and (*c*) show meridional sections (r, z) illustrating the mean radial, axial and azimuthal velocities in the *MRI* configuration for a solution computed at $R_s = 12874$. 20 contours equally distributed across $u \in [-0.15, 0.03]$, $w \in [-0.17, 0.17]$ and $v \in [0.06, 0.78]$ have been added. (*d*) Radial profiles of v computed at the same axial locations as in figure 7.

profiles near the inner cylinder might be caused by the existence of turbulent Stewartson boundary layers.

5. Discussion and conclusions

We have performed direct numerical simulations of the flow in a Taylor-Couette device that Edlund & Ji (2014) specifically designed to infer the hydrodynamic stability of constant-density Keplerian flows. A first interesting observation is that the occurrence of turbulence at low R_s appears to be a robust feature of quasi-Keplerian Taylor–Couette flows. Nevertheless, turbulence manifests itself differently depending on axial boundary conditions. In the *WR* configuration, as well as in the *HTX* and *MRI* configurations if the boundary conditions are not optimal, as in Ji *et al.* (2006), the end plates drive a large-scale EC which gives rise to strongly turbulent boundary layers at the cylinders. In contrast, when the *HTX* configuration is operated under optimal boundary conditions, the EC and associated turbulence is localised near the end plates.

As R_s increases turbulence localises to thin boundary layers, whereas the flow in the bulk becomes nearly azimuthal and axially uniform. The progressive relaminarisation of the bulk flow observed in these configurations does not however imply that they are all adequate to infer the stability of astrophysical flows. As reported in Edlund & Ji (2015), the azimuthal velocity profiles achieved in the *WR* configuration differ substantially from a quasi-Keplerian profile, even in their optimal regime of operation, whereas laminar Couette profiles can be realized in the *HTX* configuration with optimal boundary conditions. Leclercq *et al.* (2016) showed that quasi-Keplerian profiles can also be achieved in experiments if stable stratification is added near the end plates. However, this method becomes impractical for the large Reynolds numbers investigated in the Princeton experiments.

It is remarkable that in spite of the nearly one order of magnitude gap in Reynolds numbers between our simulations and the experiments of Edlund & Ji (2015), the az-

imuthal velocity profiles are indistinguishable. This suggests that, despite the turbulent boundary layers, the velocity profiles exhibit self-similar behaviour, in agreement with the observations Edlund & Ji (2015). Taken together, these results show that isothermal constant density quasi-Keplerian Taylor–Couette flows are stable at least up to $R_s = \mathcal{O}(10^6)$. Noteworthy, for $\eta = 0.3478$ and $Re = 10^6$ the energy of disturbances imposed to the laminar flow can be transiently amplified up to a factor of $G = 408$ (see eq. (5.1) in Maretzke *et al.* 2014). Hence it seems that for quasi-Keplerian flows linear transient growth is a poor indicator of turbulence transition.

Our results highlight that experiments of astrophysical flows cannot only rely on measuring velocity fluctuations alone, because vanishing Reynolds stresses do not imply quasi-Keplerian velocity profiles. Similarly, torque measurements are inadequate because they cannot be used to infer the level of turbulence in the bulk, which may be laminar despite highly turbulent boundary layers.

We remark that the experiments simulated here were performed with a constant density fluid, whereas in accretion disks the gas is strongly stratified in the axial and radial directions. Hence the results shown here apply to barotropic gases only. For stratified quasi-Keplerian flows several instabilities have been reported. Examples are the stratorotational instability (Molemaker *et al.* 2001; Le Bars & Le Gal 2007), the radiative instability (Le Dizès & Riedinger 2010; Riedinger *et al.* 2011), the zombie vortex instability (Marcus *et al.* 2015; Lesur & Latter 2016), the vertical shear instability (Urpin & Brandenburg 1998; Nelson *et al.* 2013) and the subcritical global instability (Klahr & Bodenheimer 2003; Johnson & Gammie 2006; Petersen *et al.* 2007). The ability to realize quasi-Keplerian velocity profiles in experiments at large Reynolds numbers opens up avenues for new experimental investigations of some of these instabilities and their underlying mechanisms. Candidates are the vertical shear instability or subcritical global instability, which could be addressed with experiments of radially stratified Taylor–Couette flows including thermal relaxation, or the zombie vortex instability, which could be studied in a Taylor–Couette setup subject to strong stable stratification in the vertical direction. Nevertheless, additional issues related to the interplay between end plates and stratification must be first addressed (Lopez *et al.* 2015).

We are grateful to red Española de Supercomputación (RES) and the Regionales Rechenzentrum Erlangen (RRZE) for the computational resources provided.

REFERENCES

Avila, M. 2012 Stability and angular-momentum transport of fluid flows between corotating cylinders. *Phys. Rev. Lett.* **108**.

Avila, M., Grimes, M., Lopez, J. M. & Marques, F. 2008 Global endwall effects on centrifugally stable flows. *Phys. Fluids* **20**, 104104.

Balbus, S. A. 2003 Enhanced angular momentum transport in accretion disks. *Annual Review of Astronomy and Astrophysics* **41** (1), 555–597.

Balbus, S. A. & Hawley, J. F. 1998 Instability, turbulence, and enhanced transport in accretion disks. *Rev. Mod. Phys.* **70**, 1–53.

Brauckmann, H. J. & Eckhardt, B. 2013 Direct numerical simulations of local and global torque in taylor–couette flow up to re= 30 000. *Journal of Fluid Mechanics* **718**, 398–427.

Dubrulle, B., Dauchot, O., Daviaud, F., Longaretti, P.-Y., Richard, D. & Zahn, J.-P. 2005*a* Stability and turbulent transport in taylor couette flow from analysis of experimental data. *Physics of Fluids* **17** (9).

Dubrulle, B., Marié, L., Normand, C., Richard, D., Hersant, F. & Zahn 2005*b* A hydrodynamic shear instability in stratified disks. *Astronomy & Astrophysics* **429**, 1–13.

Edlund, E. M. & Ji, H. 2014 Nonlinear stability of laboratory quasi-keplerian flows. *Phys. Rev. E* **89**, 021004.

Edlund, E. M. & Ji, H. 2015 Reynolds number scaling of the influence of boundary layers on the global behavior of laboratory quasi-keplerian flows. *Phys. Rev. E* **92**, 043005.

Fricke, K. 1968 Instabilität stationärer Rotation in Sternen. *Zeitschrift fr Astrophysik* **68**, 317.

Goldreich, P. & Schubert, G. 1967 Differential Rotation in Stars. *Astrophys. J.* **150**, 571.

Hollerbach, R. & Fournier, A. 2004 End-effects in rapidly rotating cylindrical taylor-couette flow. In *MHD Couette Flows: Experiments and Models*, , vol. 733, pp. 114–121. AIP Conference Proceedings.

Hughes, S. & Randriamampianina, A. 1998 An improved projection scheme applied to pseudospectral methods for the incompressible Navier-Stokes equations. *Intnl J. Num. Meth. Fluids* **28**, 501–521.

Ji, H. & Balbus, S. 2013 Angular momentum transport in astrophysics and in the lab. *Physics Today* **66** (8), 27–33.

Ji, H., Burin, M., Schartman, E. & Goodman, J. 2006 Hydrodynamic turbulence cannot transport angular momentum effectively in astrophysical disks. *Nature* **444** (7117), 343–346.

Johnson, B. M. & Gammie, C. F. 2006 Nonlinear stability of thin, radially stratified disks. *The Astrophysical Journal* **636** (1), 63.

Kerswell, R. 2015 Instability driven by boundary inflow across shear: a way to circumvent rayleigh's stability criterion in accretion disks? *Journal of Fluid Mechanics* **784**, 619–663.

Klahr, H. & Bodenheimer, P. 2003 Turbulence in accretion disks: Vorticity generation and angular momentum transport via the global baroclinic instability. *The Astrophysical Journal* **582** (2), 869.

Le Bars, M. & Le Gal, P. 2007 Experimental analysis of the stratorotational instability in a cylindrical couette flow. *Physical review letters* **99** (6), 064502.

Le Dizès, S. & Riedinger, X. 2010 The strato-rotational instability of taylor–couette and keplerian flows. *Journal of Fluid Mechanics* **660**, 147–161.

Leclercq, C., Partridge, J. L., Augier, P., Dalziel, S. B. & Kerswell, R. R. 2016 Using stratification to mitigate end effects in quasi-keplerian taylor–couette flow. *Journal of Fluid Mechanics* **791**, 608–630.

Lesur, G. & Latter, H. 2016 On the survival of zombie vortices in protoplanetary discs. *Monthly Notices of the Royal Astronomical Society* **462**, 4549–4554.

Lin, D. N. C. & Papaloizou, J. 1980 On the structure and evolution of the primordial solar nebula. *Monthly Notices of the Royal Astronomical Society* **191** (1), 37–48.

Lin, D. N. C. & Pringle, J. E. 1987 A viscosity prescription for a self-gravitating accretion disc. *Monthly Notices of the Royal Astronomical Society* **225** (3), 607–613.

Lopez, J. M. & Marques, F. 2015 Dynamics of axially localized states in taylor-couette flows. *Phys. Rev. E* **91**, 053011.

Lopez, J. M., Marques, F. & Avila, M. 2015 Conductive and convective heat transfer in fluid flows between differentially heated and rotating cylinders. *International Journal of Heat and Mass Transfer* **90**, 959 – 967.

Lopez, J. M. & Shen, J. 1998 An efficient spectral-projection method for the Navier-Stokes equations in cylindrical geometries I. Axisymmetric cases. *J. Comput. Phys.* **139**, 308–326.

Marcus, P., Pei, S., Jiang, C., Barranco, J., Hassanzadeh, P. & Lecoanet, D. 2015 Zombie vortex instability. i. a purely hydrodynamic instability to resurrect the dead zones of protoplanetary disks. *The Astrophysical Journal* **808** (1), 87.

Maretzke, S., Hof, B. & Avila, M. 2014 Transient growth in linearly stable taylor-couette flows. *J. Fluid Mech.* **742**, 254–290.

Mercader, I., Batiste, O. & Alonso, A. 2010 An efficient spectral code for incompressible flows in cylindrical geometries. *Computers & Fluids* **39**, 215–224.

Miesch, M., Matthaeus, W., Brandenburg, A., Petrosyan, A., Pouquet, A., Cambon, C., Jenko, F., Uzdensky, D., Stone, J., Tobias, S., Toomre, J. & Velli, M. 2015 Large-eddy simulations of magnetohydrodynamic turbulence in heliophysics and astrophysics. *Space Science Reviews* **194** (1), 97–137.

Molemaker, M. J., McWilliams, J. C. & Yavneh, I. 2001 Instability and equilibration of centrifugally stable stratified taylor-couette flow. *Physical review letters* **86** (23), 5270.

Nelson, R. P., Gressel, O. & Umurhan, O. M. 2013 Linear and non-linear evolution of the vertical shear instability in accretion discs. *Monthly Notices of the Royal Astronomical Society* p. stt1475.

Nordsiek, F., Huisman, S. G., van der Veen, R. C. A., Sun, C., Lohse, D. & Lathrop, D. P. 2015 Azimuthal velocity profiles in rayleigh-stable taylorcouette flow and implied axial angular momentum transport. *Journal of Fluid Mechanics* **774**, 342–362.

Obabko, A., Cattaneo, F. & Fischer, P. 2008 The influence of horizontal boundaries on ekman circulation and angular momentum transport in a cylindrical annulus. *Physica Scripta* **T132**, 014029.

Paoletti, M., van Gils, D. P., Dubrulle, B., Sun, C., Lohse, D. & Lathrop, D. 2012 Angular momentum transport and turbulence in laboratory models of keplerian flows. *Astronomy & Astrophysics* **547**, A64.

Paoletti, M. S. & Lathrop, D. P. 2011 Angular momentum transport in turbulent flow between independently rotating cylinders. *Physical review letters* **106** (2), 024501.

Petersen, M., Julien, K. & Stewart, G. 2007 Baroclinic vorticity production in protoplanetary disks. *The Astrophysical Journal* **658**, 1236–1251.

Ravelet, F., Delfos, R. & Westerweel, J. 2010 Influence of global rotation and reynolds number on the large-scale features of a turbulent taylorcouette flow. *Physics of Fluids* **22** (5).

Rayleigh, L. 1917 On the dynamics of revolving fluids. *Proc. Roy. Soc. Lond. A* **93** (648), 148–154.

Richard, D. & Zahn, J.-P. 1999 Turbulence in differentially rotating flows. what can be learned from the couette-taylor experiment. *Astronomy & Astrophysics* **347**, 734–738.

Riedinger, X., Le Dizès, S. & Meunier, P. 2011 Radiative instability of the flow around a rotating cylinder in a stratified fluid. *Journal of Fluid Mechanics* **672**, 130–146.

Ryu, D. & Goodman, J. 1992 Convective instability in differentially rotating disks. *Astrophys. J.* **388**, 438–450.

Schartman, E., Ji, H., Burin, M. J. & Goodman, J. 2012 Stability of quasi-keplerian shear flow in a laboratory experiment. *Astronomy & Astrophysics* **543**, A94.

Shalybkov, D. & Rüdiger, G. 2005 Stability of density-stratified viscous taylor-couette flows. *AA* **438** (2), 411–417.

Shi, L., Rampp, M., Hof, B. & Avila, M. 2015 A hybrid mpi-openmp parallel implementation for pseudospectral simulations with application to taylorcouette flow. *Computers & Fluids* **106**, 1 – 11.

Toomre, A. 1964 On the gravitational stability of a disk of stars. *The Astrophysical Journal* **139**, 1217–1238.

Turner, N. J., Fromang, S., Gammie, C., Klahr, H., Lesur, G., Wardle, M. & Bai, X. N. 2014 Transport and accretion in planet-forming disks. *Arizona University press* .

Urpin, V. & Brandenburg, A. 1998 Magnetic and vertical shear instabilities in accretion discs. *Monthly Notices of the Royal Astronomical Society* **294**, 399.